RSC Publishing Faraday Discussions

# Observation of multi-channel non-adiabatic dynamics in aniline derivatives using time-resolved photoelectron imaging



| | |
|---|---|
| Journal: | *Faraday Discussions* |
| Manuscript ID | FD-ART-04-2016-000092.R1 |
| Article Type: | Paper |
| Date Submitted by the Author: | 23-May-2016 |





| | |
|---|---|
| Complete List of Authors: | Zawadzki, Magdalena; Heriot-Watt University, Institute of Photonics & Quantum Sciences<br>Candelaresi, Marco; Heriot-Watt University, Institute of Photonics & Quantum Sciences<br>Saalbach, Lisa; Heriot-Watt University, Institute of Photonics & Quantum Sciences<br>Crane, Stuart; Heriot-Watt University, Institute of Photonics & Quantum Sciences<br>Paterson, Martin; Heriot-Watt University, Institute Of Chemical Sciences<br>Townsend, David; Heriot-Watt University, Institute of Photonics & Quantum Sciences |

# Observation of multi-channel non-adiabatic dynamics in aniline derivatives using time-resolved photoelectron imaging

Magdalena M. Zawadzki[1], Marco Candelaresi[1], Lisa Saalbach[1], Stuart W. Crane[1], Martin J. Paterson[2] and Dave Townsend[1,2,a)]

[1] *Institute of Photonics & Quantum Sciences, Heriot-Watt University, Edinburgh, EH14 4AS, United Kingdom*

[2] *Institute of Chemical Sciences, Heriot-Watt University, Edinburgh, EH14 4AS, United Kingdom*

## Abstract

We present results from a recent time-resolved photoelectron imaging (TRPEI) study investigating the non-adiabatic relaxation dynamics of *N*,*N*-dimethylaniline (*N*,*N*-DMA) and 3,5-dimethylaniline (3,5-DMA) following excitation at 240 nm. Analysis of the experimental data is supported by *ab initio* coupled-cluster calculations evaluating excited state energies and the evolution of several excited state physical properties as a function of N–H/N-$CH_3$ bond extension – a critical reaction coordinate. The use of site-selective methylation brings considerable new insight to the existing body of literature concerning photochemical dynamics in the related system aniline at similar excitation wavelengths. The present work also builds on our own previous investigations in the same species at 250 nm. The TRPEI method provides highly differential energy- and angle-resolved data and, in particular, the temporal evolution of the photoelectron angular distributions afforded by the imaging approach offers much of the new dynamical information. In particular, we see no clear evidence of the second excited $2\pi\pi^*$ state non-adiabatically coupling to the lower-lying $S_1(\pi\pi^*)$ state or the mixed Rydberg/valence $S_2(3s/\pi\sigma^*)$ state. This, in turn, potentially raises some unresolved questions about the overall nature of the dynamics operating in these systems, especially in regard to the $2\pi\pi^*$ state's ultimate fate. More generally, the findings for the aromatic systems *N*,*N*-DMA and 3,5-DMA, taken along with our recent TRPEI results for several aliphatic amine species, highlight interesting questions about the nature of electronic character evolution in mixed Rydberg-valence states as a function of certain key bond extensions and the extent of system conjugation. We begin exploring these ideas computationally for a systematically varied series of tertiary amines.

[a] Corresponding Author. E-mail: D.Townsend@hw.ac.uk

## I. INTRODUCTION

Amine-based motifs are an integral component within a variety of biological molecules including the DNA bases, amino acids and phenylpropanoids in plants.[1, 2] It is therefore of great interest to fully study and understand the physical and chemical role of these sub-units within the larger biological environment. One important characteristic of these species is the relaxation dynamics they exhibit following ultraviolet (UV) irradiation. UV absorption is potentially harmful to living organisms, and the ability of biological chromophores to non-radiatively dissipate this excess energy harmlessly into the surrounding environment via efficient ultrafast non-adiabatic processes has attracted much recent study.[3, 4] This provides a critical "photostability" that may have been an important evolutionary factor in the development of early life 3.5 billion years ago – particularly as the surface of the Earth was subject to much harsher UV irradiation conditions at that time due to the atmosphere not yet being fully developed.[5]

The aniline molecule is a good example of a system that has been used as a starting model to begin exploring the links between chemical structure, non-adiabatic dynamics and thus the photostability function of larger, biologically relevant molecules. Over the past decade several experimental studies, complemented by in-depth theoretical investigations, have been undertaken using a range different methodologies and associated observables.[6-14] This body of literature includes our own previously published results, obtained using the time-resolved photoelectron imaging (TRPEI) technique, which interrogated the relaxation dynamics of gas-phase aniline at UV excitation wavelengths in the region 273-266 nm (close to the origin of the $S_2$ excited state – characterised in more detail below) and also at 250 nm.[6, 9] In the latter study we also reported findings for the structurally related species *N*,*N*-dimethylaniline (*N*,*N*-DMA) and 3,5-dimethylaniline (3,5-DMA), which are shown in Fig. 1 along with their UV absorption spectra. This use of site-selective methylation afforded

considerable new dynamical insight – especially given previous work on aniline had implicated motion along the N-H stretching coordinate and deformations of the aromatic ring structure as being critical to access conical intersections that mediate the overall relaxation process following UV excitation.[8, 12, 14] The two lowest-lying singlet excited electronic states in aniline, *N*,*N*-DMA and 3,5-DMA may be designated $S_1(\pi\pi^*)$ and $S_2(3s/\pi\sigma^*)$. Following single-photon excitation at 250 nm, these are the only two states that are energetically accessible and both may be prepared optically. In the Franck-Condon region, the $S_2$ state is predominantly 3s Rydberg in nature, while at extended N-H bond lengths (N-$CH_3$ in the case of *N*,*N*-DMA) this rapidly evolves towards πσ* valence character. In aniline and *N*,*N*-DMA, population loss from the initially prepared $S_2(3s/\pi\sigma^*)$ state was determined to occur via two competing ultrafast (<100 fs) mechanisms: internal conversion to the (much longer-lived) $S_1(\pi\pi^*)$ state or, alternatively, direct dissociation along the N-X stretching coordinate (X = H or $CH_3$). In 3,5-DMA, however, direct N-H dissociation was inferred to be the only significant relaxation pathway due to methylation of the aromatic ring system significantly slowing down the timescale for the system to reach the $S_2(3s/\pi\sigma^*)/S_1(\pi\pi^*)$ conical intersection (CI) and undergo efficient internal conversion. Of particular importance to our analysis was the highly-differential information revealed in the temporal evolution of the photoelectron angular distributions (PADs) provided by the imaging aspect of the TRPEI approach. We therefore now seek to extend the same methodology to shorter excitation wavelengths and consider the non-adiabatic dynamics that operate in *N*,*N*-DMA and 3,5-DMA following 240 nm excitation. As explored in some detail previously, these systems exhibit very similar electronic state characters and energies as aniline.[6] As seen in Fig. 1, at 240 nm, there is now a clear onset of strong absorption to a higher-lying state, assigned (in aniline) as having singlet ππ* character.[8, 12, 15, 16] Several Rydberg states have, however, been predicted to sit slightly below this ππ* state in energy.[6, 17] In order to avoid any confusion

relating to state ordering, we therefore simply denote this second ππ* state as 2ππ* throughout. Literature summaries of the photochemical dynamics studies undertaken in aniline at absorption wavelengths >240 nm have been reported in our previous work.[6, 9] As such, only details of direct relevance to the present study (involving 2ππ* excitation) are briefly highlighted below.

Ashfold and co-workers have thoroughly investigated the mechanisms of H atom loss in aniline following UV excitation using photofragment translational spectroscopy.[14] Upon incrementally reducing the excitation wavelength from 250 nm to 193.3 nm, these authors observed distinct changes in H atom total kinetic energy release spectra, attributed to the onset of excitation to the 2ππ* state at ~240 nm. Subsequent non-adiabatic decay through a 2ππ*/$S_2$(3s/πσ*) CI or via successive 2ππ*/$S_1$(ππ*) and $S_1$(ππ*)/$S_2$(3s/πσ*) CIs was suggested, yielding H atom photoproducts with high kinetic energies formed via dissociation on the $S_2$(3s/πσ*) state potential surface. Additionally, competing decay of 2ππ* population via a CI with the $S_0$ ground state was invoked to account for a lower energy TKER component seen in the data. A more recent time-resolved ion-yield study of aniline by Montero *et al.* has, in agreement with Ashfold and co-workers, concluded that excitation to the 2ππ* state has become an open channel at 240 nm and also suggested similar relaxation pathways to those proposed previously.[13] Stavros and co-workers subsequently explored the ultrafast dynamics in photoexcited aniline using time-resolved H atom imaging.[12] Once again, this work concluded that excitation 240 nm populates the 2ππ* state and supporting calculations predicted a barrierless internal conversion pathway from 2ππ* to $S_1$(ππ*) that is mediated by out-of-plane molecular deformations. Population then evolves further onto the $S_2$(3s/πσ*) excited state which undergoes ultrafast N-H bond fission. Finally, Fielding and co-workers have undertaken an intensive TRPEI investigation of the photochemistry of aniline at a range of excitation wavelengths, including the region around 240 nm. The initial findings of these

authors concluded that the 2ππ* state decays on a sub 100 fs timescale directly to the $S_0$ ground state.[10, 11] In more recent communications these authors have expanded this interpretation and invoke (based upon extensive supporting theory) a three-state conical intersection involving 2ππ*, $S_2$(3s/πσ*) and $S_1$(ππ*).[7, 8] This predominantly transfers 2ππ* population directly to the ground state although some evidence of relaxation via the $S_1$(ππ*) and/or $S_2$(3s/πσ*) states was also observed. Interestingly, this latter pathway was not directly observed in deuterated d7-aniline.

In addition to providing new insight into the dynamics that operate in aniline-based motifs (and in particular, to further exploring the dynamical role of the 2ππ* state), our present findings, along with those we have reported in several other recent TRPEI studies on related systems[18-20], begin to raise broader questions about the influence of different chemical substituents attached to the N atom centre on the exact nature of mixed Rydberg/valence development within the electronic states of amines. In addition, the physical evolution of Rydberg-to-valence character along specific molecular coordinates highlights even more general issues relating to *intra*-state detection sensitivity effects that may potentially arise in many photoionization-based experiments. This also then leads to related considerations for *inter*-state detection as population non-adiabatically evolves over multiple potential energy surfaces. The second part of this communication discusses these ideas in more detail and summarizes recent work that begins to explore them computationally for a systematically varied series of tertiary amines.

## II. EXPERIMENTAL

Our experimental TRPEI setup has been described in detail elsewhere.[21] The fundamental laser output of a 1 kHz Ti:Sapphire laser system (Spectra Physics, Spitfire Pro/Empower) operating at a central wavelength of 800 nm with 30 nm full-width-at-half-maximum (FWHM) bandwidth provided the input for a pair of optical parametric amplifier

(OPA) systems (Spectra Physics, OPA-800c and TOPAS Prime-U, Light Conversion – used for the pump and probe generation, respectively). The pump beam (240 nm, ~0.5 μJ/pulse) was obtained by two sequential non-linear processes: generation of 480 nm radiation through sum frequency mixing a portion of the fundamental 800 nm laser output with the OPA signal beam and then subsequent frequency doubling. The probe beam (308 nm, ~1.6 μJ/pulse) was obtained by twice frequency doubling the signal beam output of the second OPA. Thin β-barium borate (BBO) crystals were used as the non-linear medium throughout. The UV pump and probe beams then propagated through single-pass prism compressors (fused silica and $CaF_2$, respectively) and were combined on a dichroic mirror before being focussed into the photoelectron imaging spectrometer using a 25 cm fused silica lens. Temporal delay between the pump and probe was controlled using a motorized linear translation stage running under computer command. As seen in Fig.1, the choice of a 308 nm probe ensures our data will be free from unwanted "probe-pump" signals evolving towards negative delay times.

Liquid molecular samples were purchased from Sigma-Aldrich (*N*,*N*-DMA 99% and 3,5-DMA 98%) and used without further purification. These were used to soak small pieces of filter paper that were placed within the body of a 1 kHz pulsed molecular beam valve, directly behind the exit nozzle (Ø=150 μm).[22] Helium (1 bar) was used as carrier gas and the temperature of the valve was regulated at 45 °C using a chiller. After expansion into the source chamber of the spectrometer, samples seeded in the molecular beam passed through a skimmer (Ø=1.0 mm) and into the main interaction chamber. Here they were intersected at 90° by the (co-propagating) UV pump and probe in a region of space between the repeller and extractor electrodes of a magnetically shielded electrostatic lens assembly optimized for velocity-map imaging.[23] Photoelectrons generated from (1+1′) resonant multiphoton ionization were then guided along a short flight tube and imaged spatially using a 40 mm MCP/P47 phosphor screen detector in conjunction with CCD (640 x 480 pixels) camera.

Photoelectron images were acquired at a series of repeatedly sampled pump-probe delay positions spanning -300 fs to +500 fs in 25 fs increments and +500 fs to +50 ps in 7 exponentially increasing time steps. At each time step, pump-alone and probe-alone photoelectron images were also recorded for background subtraction. Prior to commencing photoelectron collection, the spectrometer was switched into ion detection mode and the pulsed valve timing conditions tuned to ensure no signals from clusters were observed. Compressor lengths for each beam line were also systematically adjusted to yield a cross correlation of 130 ± 10 fs, as determined from non-resonant two-colour (1+1') multiphoton ionization of pyrrole. This data also provided energy calibration information for the spectrometer.

## III. EXPERIMENTAL RESULTS

### A. Time-resolved Photoelectron Spectra

Fig. 2 presents a series of photoelectron images resulting from (1 + 1′) photoionization of *N*,*N*-DMA and 3,5-DMA at a range of selected temporal delay times between the pump (240 nm) and probe (308 nm) beams. Of particular note is the sharp, and highly anisotropic outer ring that peaks along the direction of laser polarization in the data recorded at very short delay times. Time-resolved photoelectron spectra may be generated from the complete sets of acquired image data (using appropriate energy calibration information and pixel weighting) following application of a rapid matrix inversion approach described in detail elsewhere.[21] These plots are shown in Fig. 3 (note the mixed linear-logarithmic scaling of the time axis). Both systems under study show a long-lived feature spanning the low-kinetic energy region up to ~0.8 eV. An additional feature exhibiting extremely rapid decay is also seen at higher kinetic energies. On first inspection, the overall appearance of these spectra is very similar to that seen previously following excitation at 250 nm,[6] although the high kinetic energy features

are somewhat different in shape – a consequence of direct excitation to the 2ππ* state, as expanded upon in more detail later.

The temporal evolution of the photoelectron data was analysed quantitatively using a global Levenberg-Marquardt fitting routine where the 2D experimental data $S(E, \Delta t)$ are expressed as follows:

$$S(E, \Delta t) = \sum_i A_i(E) \cdot P_i(\Delta t) \otimes g(\Delta t) \quad (1)$$

Here $A_i(E)$ is the decay associated photoelectron spectrum of the $i^{th}$ data channel, which has a time dependent population $P_i(\Delta t)$ described by a series of exponentially decaying profiles (all of which originate from zero pump-probe delay) and $g(\Delta t)$ represents the (Gaussian) experimental cross-correlation function of the pump and probe pulses. The global nature of the fitting procedure provides a series of decay associated spectra (DAS) that plot the relative amplitude of each exponential component as a function of photoelectron kinetic energy. In order to obtain a satisfactory fit to both the *N*,*N*-DMA and 3,5-DMA data using Eq. 1, a total of four exponentially decaying functions were required. We label these using their respective time constants $\tau_{1–4}$ (note that only three such functions were necessary in our equivalent analysis following 250 nm excitation). The DAS obtained are shown in Fig. 4, along with their respective time constants, which are broadly similar to those previously reported by Fielding and co-workers for aniline at similar excitation wavelengths.[7, 10, 11] To illustrate the good overall quality of the model, Fig. 3 also includes the corresponding global fit and associated residuals for the 3,5-DMA data. In both systems under study, only the $\tau_1$ and $\tau_2$ DAS contribute significant fit amplitude at relatively high photoelectron kinetic energies (>0.8 eV). The $\tau_1$ DAS describes an extremely fast decay that, within the limits of our experimental instrument response, exhibits essentially zero lifetime (i.e. the fit component was Gaussian). The $\tau_2$ DAS describes a longer decay (110-120 fs) which shows a sharp, large

amplitude feature (at 1.2 eV and 0.95 eV for *N*,*N*-DMA and 3,5-DMA, respectively) superimposed on a broader background. In regions of lower photoelectron kinetic energy (<0.8 eV), the $\tau_1$ DAS obtained for *N*,*N*-DMA does not contribute significant amplitude to the overall global fit but $\tau_{2-4}$ are still significant, with $\tau_2$ having a negative component. This is in contrast to the situation in 3,5-DMA where only $\tau_3$ and $\tau_4$ are effectively non-zero. Overall, the timescales and relative amplitudes of the various DAS associated with $\tau_{2-4}$ in the 240 nm excitation data for both *N*,*N*-DMA and 3,5-DMA are very similar to those seen previously at 250 nm.[6] The only difference at 240 nm is the inclusion of the additional Gaussian fit component $\tau_1$, which appears to have no significant influence on the behaviour on the other temporal processes observed. Given this observation we may therefore attribute the $\tau_1$ DAS directly to the decay of the 2ππ* state (which is not populated at 250 nm) and assign the $\tau_{2-4}$ DAS in accordance with our earlier work: $\tau_2$ describes decay of the $S_2(3s/\pi\sigma^*)$ state, while $\tau_3$ and $\tau_4$ represent intramolecular vibrational redistribution (IVR) within $S_1(\pi\pi^*)$ state and the ultimate long-time decay of the $S_1(\pi\pi^*)$ state, respectively. This brief summary will be expanded upon further in the Discussion. Finally, the $D_1$ ($\pi^{-1}$) vertical ionisation potentials for *N*,*N*-DMA, and 3,5-DMA are 9.00 eV, and 8.55 eV, respectively.[24, 25] Our (1 + 1′) REMPI scheme at 240/308 nm provides a total photon energy of 9.19 eV, and so ionization to the $D_1$ ($\pi^{-1}$) cation state (in addition to the $D_0$ ($\pi^{-1}$) state) may, in principle, be observed in our TRPEI data. Excitation at 240 nm (5.17 eV) is energetically well above the origins of the $S_1(\pi\pi*)$ and $S_2(3s/\pi\sigma^*)$ states[6] and so heuristic Franck-Condon arguments lead us to assume the propensity for $D_1$ ($\pi^{-1}$) ionization (with a 308 nm probe) is likely to be small in these instances. In contrast, 2ππ* is prepared closer to its electronic origin and it is perhaps therefore surprising that no amplitude is seen in the $\tau_1$ DAS (particularly for 3,5-DMA) in the low photoelectron

kinetic energy region. This possibly indicates that the $D_1$ ($\pi^{-1}$) state exhibits a somewhat different geometry to that of $D_0$ ($\pi^{-1}$).

### B. Photoelectron Angular Distributions

Additional dynamical information can be obtained from our TRPEI data by investigating the temporal evolution of the photoelectron angular distribution (PADs). For the case of a two-photon ionization using parallel linear polarizations, the PADs are described by the following mathematical form:[26, 27]

$$I(E,\Delta t,\theta)=\frac{\sigma(E,\Delta t)}{4\pi}\left[1+\beta_2(E,\Delta t)P_2(\cos\theta)+\beta_4(E,\Delta t)P_4(\cos\theta)\right] \qquad (2)$$

Here $\sigma(E, \Delta t)$ is the time-dependent photoelectron energy distribution acquired at each pump-probe delay time $\Delta t$, the $P_n(\cos\theta)$ terms are the $n^{th}$-order Legendre polynomials and $\beta_2$ and $\beta_4$ are the well-known anisotropy parameters. The angle $\theta$ = 180° is defined by a vertical line running fully through the images shown in Fig. 2 via their centre points. Fits to our PAD data using Eq. 2 reveals significant time-dependent variation of both the $\beta_2$ and $\beta_4$. Fig. 5 plots the temporal evolution of these parameters when averaged over the low kinetic energy region of the photoelectron spectra spanning 0.05-0.70 eV where long-lived (≥100 ps) signals are observed (as modelled by the $\tau_4$ DAS shown in Fig. 4). For both systems under study, the temporal variation of both $\beta_2$ and $\beta_4$ is consistent within this selected energy region and averaging only serves to improve the statistics in the data presented. Each system exhibits a clear initial rise in $\beta_2$ at short times beyond $\Delta t$ = 0. This is slightly more rapid in *N*,*N*-DMA (~100 fs) than in 3,5-DMA (~250 fs). Beyond this point in time, the two molecules differ to some extent in their behaviour. In *N*,*N*-DMA $\beta_2$ plateaus before falling again slightly after ~1 ps. In contrast, 3,5-DMA exhibits an additional increase in $\beta_2$ on a more extended timescale, reaching a maximum value in 2 ps and then remaining at this level out to 50 ps. In both

systems, the evolution of $\beta_4$ occurs in a similar manner to that seen in the corresponding $\beta_2$ values, although the initial $\beta_2$ rise seen in 3,5-DMA is accompanied by a $\beta_4$ fall. In *N*,*N*-DMA the $\beta_2$ plateau region also appears to be resolved into two distinct temporal features in the equivalent $\beta_4$ plot. The inset panels included in Fig. 5 permit a direct comparison between the temporal evolution of $\beta_2$ in our present 240 nm excitation data and that observed previously at 250 nm. In both systems, the 240 nm data appears to show a feature that is effectively superimposed on top of the behaviour seen at the longer excitation wavelength. As was the case with the DAS data described earlier, we therefore attribute these additional features to a process directly associated with the $2\pi\pi^*$ state.

At higher kinetic energies (<0.8 eV), photoelectron signals in the data are extremely short lived and no information relating to their temporal evolution may be reliably obtained. However, Fig. 5 also plots $\beta_2$ and $\beta_4$ as a function of photoelectron kinetic energy in the region close to $\Delta t = 0$, superimposed on the corresponding photoelectron spectra. It is clear that the sharp, intense photoelectron peak seen at ~1 eV in each system (also visible in $\tau_2$ DAS shown in Fig. 4) exhibits a relatively high value of $\beta_2$ but only a small value of $\beta_4$. This is strongly characteristic of the 3s Rydberg character of the $S_2(3s/\pi\sigma^*)$ state, as will be expanded upon further in the Discussion. In addition, *N*,*N*-DMA shows a pronounced and sharp increase in both $\beta_2$ and $\beta_4$ at photoelectron kinetic energies around 1.7 eV. Once again, this is characteristic of an ionization signal from a Rydberg state (presumably of 3p character – see Theory section). No obvious strong feature associated with this Rydberg state is seen in the corresponding photoelectron spectrum, suggesting it is not populated to any significant extent (or, alternatively, exhibits a very small ionization cross section). The fact that the presence of this state is revealed in the PAD data (which is effectively an "intensity

normalized" analysis) nicely illustrates a useful advantage of the imaging-based experimental approach.

## IV. THEORY: *N*,*N*-DMA and 3,5-DMA

Potential energy surface cuts along the N-$CH_3$ and N-H stretching coordinates were obtained for *N*,*N*-DMA and 3,5-DMA, respectively, using equation of motion (EOM) coupled cluster theory with single and double substitutions in conjunction with an aug-cc-pVDZ basis set. These coordinates have been strongly implicated as being key in mediating the overall non-adiabatic dynamics.[8, 12, 14] Vertical oscillator strengths were computed using fully relaxed linear response transition densities. Equilibrium $S_0$ geometries were taken from a B3LYP/aug-cc-pVTZ optimisation in $C_s$ symmetry. All calculations were undertaken with the Gaussian09 program.[28] The results, as summarized in Table I, are consistent with our previous work.[6] We note that the 2ππ* state is quite diffuse in character and sits energetically above several Rydberg states that have been discussed previously elsewhere.[6, 17] The oscillator strengths for transitions to the 2ππ* state are considerably larger than for $S_1$(ππ*), in agreement with the absorption spectra in Fig. 1. As seen in Fig. 6, for both *N*,*N*-DMA and 3,5-DMA all electronic states considered are strongly bound along the N-$CH_3$/N-H coordinate with the exception of $S_2$(3s/πσ*), which exhibits only a small potential barrier before tending towards a dissociative asymptote and at 240 nm direct N-$CH_3$/N-H bond fission is expected to be an energetically open pathway. At highly extended bond lengths (beyond the limits of where the coupled cluster approach begins to breakdown) a crossing between the $S_2$(3s/πσ*) state with the $S_0$ ground state is also expected, as previously shown for the closely related case of aniline.[12]

## V. DISCUSSION

As already outlined in Section III, the DAS and PAD data extracted from our TRPEI measurements point to a situation where the overall 240 nm relaxation dynamics observed in both *N*,*N*-DMA and 3,5-DMA may be viewed as a combination of decay pathways seen

previously at 250 nm and an additional process attributable to the onset of excitation to the 2ππ* state. In the case of the DAS analysis, this was strongly suggested by the similarity of the $\tau_{2-4}$ spectra seen in each molecule at the two different excitation wavelengths. In the PADs, the temporal evolution of the $\beta_2$ anisotropy parameter following 240 nm excitation appeared to be an effective superposition of features seen at 250 nm with a new, additional component. We therefore structure the Discussion by first summarizing the dynamical processes associated with the $S_2(3s/\pi\sigma^*)$ and $S_1(\pi\pi^*)$ states (described elsewhere in more detail in the context of 250 nm excitation[6]) and then consider the role of the 2ππ* state.

### A. $S_2(3s/\pi\sigma^*)/S_1(\pi\pi^*)$ Dynamics

On the basis of our previous 250 nm excitation study, the $\tau_{2-4}$ DAS in both *N*,*N*-DMA and 3,5-DMA may be assigned as follows:

Firstly, the $\tau_3$ and $\tau_4$ DAS are both associated with ionization from the $S_1(\pi\pi^*)$ state. The $\tau_3$ component (1.5 ± 0.3 ps in *N*,*N*-DMA and 2.1 ± 0.3 ps in 3,5-DMA) is assigned to IVR processes, with $\tau_4$ (150 ± 20 ps in *N*,*N*-DMA and 100 ±20 ps in 3,5-DMA) then describing the overall $S_1(\pi\pi^*)$ decay. The ultimate fate of this state is not apparent in our measurements but several possibilities suggested previously (for aniline) include fluorescence[29], intersystem crossing to lower-lying triplet states[30], or internal conversion back to the $S_0$ ground state.[8, 12] Ultrafast IVR processes have previously been implicated as playing a role in the excited states of several other aromatic species in situations where the excitation is well above the origin, as is the case here for the $S_1(\pi\pi^*)$ state. This has been expanded upon previously.[6, 21]

Secondly, the $\tau_2$ DAS (120 ± 20 fs in *N*,*N*-DMA and 110 ± 20 fs in 3,5-DMA) is attributed to the decay of the $S_2(3s/\pi\sigma^*)$ state. At photoelectron kinetic energies >0.8 eV, this appears to have the form of a sharp peak (at 1.2 eV in *N*,*N*-DMA and 0.95 eV in 3,5-DMA)

superimposed on a broader background of lower amplitude. As seen in Fig. 5, the sharp peak is associated with a relatively high value of the anisotropy parameter $\beta_2$ but a very small $\beta_4$ term. In contrast, the broader component exhibits low values of both $\beta_2$ and $\beta_4$. As confirmed theoretically in our earlier work (see also Section VI), the $S_2(3s/\pi\sigma*)$ state exhibits considerable 3s Rydberg character in the vertical Franck-Condon region and evolves $\pi\sigma^*$ valence character as the N-H (3,5-DMA) and N-$CH_3$ (*N*,*N*-DMA) bond is extended. This evolution will be extremely rapid (i.e. it is not temporally resolvable in our present measurements), but we argue that we are able to see this change in the electronic character in a *spectrally averaged* way – the 3s Rydberg component of the $S_2$ state gives rise to a narrow photoelectron peak with high $\beta_2$ anisotropy – a consequence of a strong propensity for diagonal ionisation and well-defined orbital angular momentum, respectively. Since excited states of predominantly *s*-orbital character possess little or no inherent alignment, the lack of a significant $\beta_4$ contribution to the PAD is also expected here. As the $\pi\sigma^*$ valence character of the $S_2$ state increases (at the expense of the Rydberg character) a reduction in the propensity for diagonal ionisation and less well-defined orbital angular momentum leads to a broader feature in the photoelectron spectra/$\tau_2$ DAS with lower associated PAD anisotropy – as is observed.

At photoelectron kinetic energies <0.8 eV, there is a clear difference between the $\tau_2$ DAS obtained for the two systems under consideration; *N*,*N*-DMA exhibits negative amplitude across this region, whereas 3,5-DMA shows zero amplitude. This negative amplitude in the *N*,*N*-DMA data provides a strong indication of a sequential dynamical process occurring in this system that is absent in 3,5-DMA. As described in Section III. A, all exponentials used in the global DAS fit originate from zero pump-probe delay ($\Delta t = 0$). The negative amplitude in the *N*,*N*-DMA $\tau_2$ DAS (which describes a short-lived process) is

therefore effectively compensating for the positive amplitude at short delay times associated with a sequential feature (i.e., one not truly originating from $\Delta t = 0$) described by a longer-lifetime DAS in the same energy region (which in this case is the $\tau_3/\tau_4$ DAS associated with ionization from the $S_1(\pi\pi^*)$ state). Physically, this may be interpreted as a transfer of $S_2(3s/\pi\sigma^*)$ state population in *N*,*N*-DMA to the $S_1(\pi\pi^*)$ state via internal conversion. The apparent absence of this internal conversion process in 3,5-DMA means that a different, but still extremely rapid mechanism is responsible for $S_2(3s/\pi\sigma^*)$ decay in this instance. Our TRPEI measurement is effectively "blind" to this alternative pathway, but we may assume that it is direct dissociation along the N‑H stretching coordinate within the excited state, as evidenced by observations of H atom release occurring on a very rapid time scale in aniline at similar excitation wavelengths.[12, 14] This is also strongly suggested by the dissociative nature of the $S_2(3s/\pi\sigma^*)$ state revealed in our supporting calculations (see Fig. 6) which, additionally, show that an equivalent N-$CH_3$ fragmentation pathway in *N*,*N*-DMA should be possible (noting that at 240 nm we are exciting well above any small barrier present along this dissociative coordinate). In *N*,*N*-DMA we therefore appear to have the possibility of two competing $S_2(3s/\pi\sigma^*)$ decay pathways; $S_1(\pi\pi^*)$ internal conversion and $CH_3$ elimination, whereas in 3,5-DMA H atom elimination is overwhelmingly dominant. Further evidence for this is clearly revealed in the PAD data, as described below.

Non-adiabatic coupling interactions between different states effectively mixes their electronic (or vibronic) character and this may be reflected in the temporal evolution of the PADs observed in a TRPEI measurement.[31-33] As discussed in Section III. B (and illustrated in Fig. 5), the temporal evolution of the anisotropy parameters at low photoelectron kinetic energies following 240 nm excitation of *N*,*N*-DMA and 3,5-DMA may be regarded as a superposition of behaviour seen at 250 nm and a new additional component which is

attributed to 2ππ* excitation. Here the PADs associated with low kinetic energy photoelectrons directly reflect the electronic character of the $S_1(\pi\pi^*)$ state. Any evolution of $\beta_2$ and $\beta_4$ may be assumed (as a first approximation[34]) to arise as a consequence of this state sampling nuclear geometries that then significantly change the electronic character (for example, geometries close to conical intersections). Upon comparing the $\beta_2$ data in Fig. 5 for 240 nm excitation (main plot) and 250 nm excitation (inset panel), it is apparent that the temporal evolution in the PADs associated with accessing the $S_1(\pi\pi^*)/S_2(3s/\pi\sigma^*)$ CI geometry is considerably slower in 3,5-DMA (~1.5 ps) than in *N*,*N*-DMA (~150 fs). Such an observation is therefore consistent with *N*,*N*-DMA exhibiting competing internal conversion and $CH_3$ elimination decay pathways for the $S_2(3s/\pi\sigma^*)$ state as the timescales for the two processes are likely to be similar. In contrast, methylation of the aromatic ring system in 3,5-DMA slows down the time to access the $S_1(\pi\pi^*)/S_2(3s/\pi\sigma^*)$ CI sufficiently that the faster H atom elimination channel becomes overwhelmingly favoured.

As demonstrated above, being able to use the PAD data afforded by the TRPEI technique to resolve such intramolecular kinetics in more detail provides a useful demonstration of the value the imaging approach brings to the study of ultrafast dynamics. In spite of this, however, we highlight one key piece of information we have so far unable to comment on: for the case of *N*,*N*-DMA we are unable to quantify the relative branching of the internal conversion and direct dissociation channels. Upon first inspection of the $\tau_2$ DAS (associated with the decay of the $S_2(3s/\pi\sigma^*)$ state), one may initially conclude that the relative sizes of the (large) positive amplitude feature and the (much smaller) negative amplitude feature implies that internal conversion is a relatively minor pathway. However, the negative amplitude component is effectively associated with ionization from the $S_1(\pi\pi^*)$ once internal conversion from $S_2(3s/\pi\sigma^*)$ has taken place. As discussed in previous work, we may

(conservatively) assume that the relative ionization cross section of the $S_2(3s/\pi\sigma^*)$ state is at least an order of magnitude larger than $S_1(\pi\pi^*)$.[6] As such, the small negative amplitude seen in the low-energy region of the $\tau_2$ DAS is therefore likely to describe a relatively large fraction of population transfer from the $S_2(3s/\pi\sigma^*)$ state (i.e we may speculate that internal conversion is likely to be the dominant pathway). We also note, however, that the much smaller absorption cross section exhibited by $S_2(3s/\pi\sigma^*)$ (relative to $S_1(\pi\pi^*)$ – see Table I) means that the initial population prepared in this state is only a very small contribution to the overall excitation process. A more detailed discussion of issues relating to *inter*-state detection sensitivity when using ionization detection to track non-adiabatic dynamics evolving over multiple potential energy surfaces is beyond the scope of this communication and the reader is directed to our previous work for a more expanded (albeit exploratory) discussion.[6, 35]

### B. 2ππ* Dynamics and Comparison with Aniline

As already discussed, the $\tau_1$ DAS seen in Fig. 4 is assigned to ionization from the $2\pi\pi^*$ state. The lifetime of this state is extremely rapid, effectively being described by a Gaussian in our global fitting model. The lack of negative amplitude in any region of the $\tau_1$ DAS also appears to suggest that the decay of the $2\pi\pi^*$ state in both *N*,*N*-DMA and 3,5-DMA does not involve population transfer to either the $S_1(\pi\pi^*)$ or $S_2(3s/\pi\sigma^*)$ states (see the argument already outlined in the previous section regarding negative DAS). Initially, this is perhaps a surprising outcome as in the related species aniline, a CI connecting all three states has been predicted and direct evidence for internal conversion from $2\pi\pi^*$ to the $S_1(\pi\pi^*)/S_2(3s/\pi\sigma^*)$ states has been reported from experimental TRPEI data following 238 nm excitation (where negative amplitude is seen in the low energy region of the DAS corresponding to that labelled $\tau_1$ here).[7] As was the case for the decay of the $S_2(3s/\pi\sigma^*)$, however, this may be rationalized

through consideration of the PAD data in Fig. 5. Following 240 nm excitation in both *N*,*N*-DMA and 3,5-DMA, the temporal evolution of $\beta_2$ and $\beta_4$ show two distinct features, one of which we have already associated with accessing the $S_1(\pi\pi^*)/S_2(3s/\pi\sigma^*)$ CI geometry. We therefore suggest that the second feature is reflecting a different geometry within the $S_1(\pi\pi^*)$ state associated with an additional CI connecting to $2\pi\pi^*$. Although the timescale associated with the evolution of this second feature is relatively fast for both species under consideration (~250 fs and ~350 fs for *N*,*N*-DMA and 3,5-DMA, respectively) it is still much longer than the observed $2\pi\pi^*$ lifetime (as described by the Gaussian $\tau_1$ DAS). In both systems we may therefore infer that (i) although decay of the $2\pi\pi^*$ state via the $S_1(\pi\pi^*)$ and/or $S_2(3s/\pi\sigma^*)$ states may be possible in principle, such a process is unable to compete kinetically with an alternative decay pathway (discussed below) and (ii) the $S_1(\pi\pi^*)$ and $S_2(3s/\pi\sigma^*)$ must therefore be populated to some extent in the initial 240 nm excitation (an assumption already implicitly assumed in the discussion presented in Section V. A). As mentioned above, this dynamical behaviour is in contrast to the situation in aniline following excitation at similar wavelengths, where internal conversion from $2\pi\pi^*$ to $S_1(\pi\pi^*)$ and/or $S_2(3s/\pi\sigma^*)$ does operate to some extent. Furthermore, it is also interesting to note that fully deuterated d7-aniline appears (on the basis of the DAS data reported by Fielding and co-worker[7]) to revert back to overall dynamical behaviour that is very similar to that seen in *N*,*N*-DMA (i.e. population transfer between the $S_2(3s/\pi\sigma^*)$ and $S_1(\pi\pi^*)$ states but *no* population transfer to either of these from $2\pi\pi^*$). This suggests that competition between different $2\pi\pi^*$ decay pathways is extremely sensitive to the vibrational timescales operating within these systems. Finally, it is worth highlighting here that in aniline, $\beta_2$ has been previously shown to undergo no temporal evolution in the low photoelectron kinetic energy region (0.2-0.4 eV) following 240 nm excitation.[36] This provides additional support to our kinetic arguments, as we assume this is a

consequence of aniline being able to access the CI geometry connecting the 2ππ* state to the $S_1(\pi\pi^*)$ and/or $S_2(3s/\pi\sigma^*)$ states on a timescale that is too fast to observe within the temporal experimental resolution – and so internal conversion to these states from 2ππ* is able to now compete with other decay mechanisms. This is also seen to be the case for the CI connecting the $S_1(\pi\pi^*)$ and $S_2(3s/\pi\sigma^*)$ in aniline following 250 nm excitation.[6]

In both *N*,*N*-DMA and 3,5-DMA, the kinetic picture outlined above for predominant 2ππ* decay via a pathway other than internal conversion to $S_1(\pi\pi^*)$ and/or $S_2(3s/\pi\sigma^*)$ appears consistent with the geometry of a 3-state $S_1(\pi\pi^*)/S_2(3s/\pi\sigma^*)/2\pi\pi^*$ CI predicted theoretically in aniline by Sala *et al*.[8] and also, alternatively, the $S_1(\pi\pi^*)/2\pi\pi^*$ CI proposed by Stavros and co-workers.[12] Both require significant motion of the $NH_2$ group out of the ring plane and some additional distortion of the ring system itself. The work of Sala *et al*. also suggests that decay of the 2ππ* state may also proceed via two other possible (barrierless) CI pathways, both of which connect the 2ππ* and $S_0$ ground states. One of these is suggested to first pass through the aforementioned 3 state CI (and so may possibly be ruled out in *N*,*N*-DMA and 3,5-DMA on the basis of our previous kinetic arguments) and the second samples a geometry similar to the Dewar form of benzene. This latter process once again requires considerable out of (ring) plane motion of the $NH_2$ group and also significant distortion of the aromatic system. In light of this, it is perhaps surprising that we are unable to resolve any significant differences in 2ππ* lifetime between *N*,*N*-DMA, 3,5-DMA and aniline (which has been recently reported as 50 ± 10 fs[7]). While such lifetime differences (beyond the temporal resolution of our present experiment) may exist, we also tentatively suggest that our findings open up the possibility that a 2ππ* decay pathway other than internal conversion to $S_0$ may be operating. Since our TRPEI experiment is effectively blind to this pathway, this remains an open question, but we note that our excited state calculations for *N*,*N*-DMA and 3,5-DMA (see Table I) and also

previously for aniline[6, 17] appear to suggest the presence of several Rydberg states sitting energetically just below the 2ππ* state (in the Franck-Condon region). As suggested theoretically by Worth and co-workers[17], a consideration of the coupling interactions between these Rydberg states and 2ππ* is necessary to model the aniline absorption spectrum satisfactorily. It therefore seems entirely possible that this interaction may also play a role in the excited state dynamics more generally. As seen in the plots of $\beta_2$ and $\beta_4$ *vs* photoelectron kinetic energy at $\Delta t$=0 presented in Fig. 5 (see also Section III. B), some spectral signatures of a p-Rydberg state do appear to be evident (at least in *N*,*N*-DMA) and so this is an avenue that warrants further investigation. Since our present experimental findings clearly illustrate the value in using highly-differential imaging methods in conjunction with systematic, site-selective substitution to study complex ultrafast non-adiabatic dynamics, we anticipate that further studies in a similar vein will prove instructive in this regard.

Finally, we once again return to the issue of relative detection sensitivity when using ionization detection to track dynamical processes involving multiple potential energy surfaces. On the basis of both the absorption spectra presented in Fig. 1 and also the oscillator strength data presented in Table I, it is extremely surprising that photoelectron signals associated with 2ππ* state ionization in both *N*,*N*-DMA and 3,5-DMA ($\tau_1$ DAS in Fig. 4) are similar/smaller in size to those attributed to the $S_2$(3s/πσ*) and $S_1$(ππ*) states ($\tau_2$ DAS and $\tau_4$ DAS, respectively). Since the 2ππ* state clearly exhibits a vastly stronger absorption, this initially suggests that it must therefore have (i) a greatly reduced (electronic) ionization cross-section (compared to the $S_2$(3s/πσ*) and $S_1$(ππ*) states) and/or (ii) very small Franck-Condon factors (within the limits imposed by 308 nm ionization). In regard to point (i), we have previously employed correlations between photoionization cross-sections and isotropic polarizability volume $< \bar{\alpha} >$ as a useful heuristic tool in assisting the interpretation of TRPEI

data.[6, 35] Although a somewhat speculative approach, we note that evaluation of $<\overline{\alpha}>$ for the 2ππ* and $S_1(\pi\pi^*)$ states of *N*,*N*-DMA (at the equilibrium geometry) suggests that the ionization cross section of the 2ππ* is, in fact, likely to be somewhat *larger* than $S_1(\pi\pi^*)$.[37] In considering point (ii), we note that the $\tau_1$ DAS shown in Fig. 4 does not appear to extend all the way to the predicted (1+1′) energy cut-off, indicating that we are at least sampling the full Franck-Condon progression. We therefore suggest that an alternative explanation is possibly responsible for much of the huge reduction seen in the relative amplitude of the $\tau_1$ DAS over what might reasonably be expected. Specifically, this is the extremely short lifetime of the 2ππ* state relative to the temporal duration of the ionizing laser pulse (~80-100 fs), which leads to a significant reduction in effective ionization efficiency relative to the $S_2(3s/\pi\sigma^*)$ and $S_1(\pi\pi^*)$ states (which have lifetimes comparable to or greatly in excess of the laser pulse duration). This conclusion (which may obviously be confirmed by conducting experiments with temporally shorter laser pulses) potentially highlights an important additional convoluting factor that may, in some cases, need be taken into consideration when attempting to interpret relative branching ratios in time-resolved experiments using photoionization detection.

## VI. GENERAL FUNCTIONALLITY EFFECTS IN AMINE RYDBERG/VALENCE EVOLUTION

As discussed in detail above, the evolution of 3s Rydberg to σ* valence character within the $S_2$ states of both *N*,*N*-DMA and 3,5-DMA is clearly an important process in mediating some aspects of the overall relaxation dynamics in these systems following UV excitation. More generally, similar Rydberg-to-valence behaviour has also been strongly implicated in playing a key role in the excited state photochemistry observed in numerous small hetero-atom containing systems. The study of such processes has therefore attracted a

great deal of attention over the last decade.[3, 4] Recent TRPEI measurements conducted on a series of tertiary aliphatic (i.e. unsaturated) amines have, however, suggested that the very long (>10 ps) overall excited state lifetimes seen in these systems are a consequence of the 3s state being unable to evolve σ* valence character and therefore undergo rapid decay (via N-C bond fission).[18, 19] In contrast, secondary and primary aliphatic amine species exhibit ultrafast (<<1 ps) decay of the 3s state as σ* valence character is able to develop in this instance.[20] This difference in dynamical timescales is illustrated in Fig. 7 for the case of piperidene (a secondary aliphatic amine) and *N*-methylpyrrolidine (a tertiary aliphatic amine) following 200 nm excitation. In both cases, a member of the 3p Rydberg manifold is initially populated. This undergoes rapid (<400 fs) internal conversion to the 3s state, which then exhibits a decay lifetime of <200 fs in piperidene and 160 ps in *N*-methylpyrrolidine. We stress that this profound difference in 3s lifetime does not appear to be a simple tunnelling rate effect that may arise due to the presence of any small barrier along the N-H/N-$CH_3$ stretch of the excited state potential surface. This is initially suggested by the fact that, following 200 nm excitation, the 3s states of both molecules are prepared (conservatively) at least 0.6 eV above their electronic origins. Exploring this in more detail computationally, calculations obtained using both the EOM-CCSD and CASSCF levels of theory indicate that there are clear general differences in the way that tertiary and secondary/primary aliphatic amines evolve valence character within their Rydberg states.[18-20] In both classes of molecule, members of the 3p manifold (but not the 3s state) appear to develop σ* valence character along N-C bond extensions (a factor responsible for mediating the 3p to 3s internal conversion mentioned above). In contrast, 3s to σ* evolution is seen along N-H coordinates. Although an interesting observation in its own right, this situation is made somewhat more confusing by the fact that the *aromatic* amines *N*,*N*-DMA (a tertiary system) and 3,5-DMA (a primary system) clearly

both exhibit dynamics consistent with the development of σ* character within the 3s Rydberg state (note also here that in Fig. 7 piperidene appears to show the same spectrally averaged ionization signatures of 3s to σ* evolution). This suggests that the presence of the aromatic ring system in *N*,*N*-DMA may exert an additional influence over the electronic state character as a function of nuclear coordinates, in turn modifying the UV relaxation dynamics.

Given the observations highlighted above, we have undertaken a preliminary theoretical investigation that begins to explore the effect of ππ* states associated with unsaturated chemical functionality on the nature of valence character evolution within the Rydberg states of amines. Fig. 8 presents a series of selected tertiary amines that systematically introduce C=C double bonds in close proximity to the amine N atom centre. For all 4 systems considered, PES cuts were evaluated along N-C bond extensions for several low-lying singlet excited states. Rigid scans were performed for the lowest energy conformer of each species. The computational approach was essentially identical to that already applied to *N*,*N*-DMA and 3,5-DMA (see Section IV) and the key results are summarized in Fig. 9. In the fully saturated system *N*,*N*-dimethylcyclohexylamine (*N*,*N*-DMCHA) we find that along the N-$CH_3$ coordinate evolution of Rydberg to (nσ*) valence character is observed from a heavily mixed p-Rydberg state lying in the quasi-molecular plane of the cyclohexane ring. At an N-C separation of ~1.9 Å this state crosses with the 3s Rydberg state, which remains strongly bound as the bond is extended. A similar scan along the N-C bond connecting to the ring system (not shown in Fig. 9) yields the same overall behaviour. Upon introducing one C=C double bond into *N*,*N*-DMCHA, three isomers are possible, and we have investigated the specific species *N*,*N*-dimethyl-1-cyclohexen-1-amine (*N*,*N*-DM-1-CHA) – chosen as it places the unsaturated functionality closest to the N atom centre. Here we once again find p-Rydberg to valence evolution, similar to the fully saturated case – although we note that the Rydberg states are extremely mixed in this system and tracking their (adiabatic) evolution as the N-C

bond extends is particularly challenging. Energetically, the lowest-lying ππ* state associated with the C=C double bond sits well above the 3s and 3p Rydberg manifold (and is not shown in the Fig. 9 plot). Increasing the complexity further, for diene systems several isomers are again possible, and we have investigated the conjugated 1,3 species *N*,*N*-dimethyl-1,3-cyclohexadien-1-amine (*N*,*N*-DM-1,3-CHA) that is additionally conjugated with the nitrogen lone pair, and the corresponding 2,4 species *N*,*N*-dimethyl-2,4-cyclohexadien-1-amine (*N*,*N*-DM-2,4-CHA) where the N atom interaction is absent. For both systems there are now two ππ* states, one embedded within the Rydberg manifold and one (that is considerably more diffuse) at much higher energies. Only the former is included in Fig. 9. In terms of the valence character evolution along the N-$CH_3$ stretch we now observe differing behaviour in these species. The nitrogen conjugated species *N*,*N*-DM-1,3-CHA exhibits less s/p Rydberg mixing, and here it is the lowest (predominantly 3s) state that evolves valence σ* character, behaviour that is now similar to the aromatic tertiary system *N*,*N*-DMA (see Fig. 6). In the case of *N*,*N*-DM-2,4-CHA, however, the s/p mixing is greater, and it is a higher notional p-Rydberg state that evolves the valence σ* character in a manner similar to both the species with zero and one double bonds in the ring, and also reminiscent of our previous tertiary aliphatic amines studies.[18, 19] Overall these are interesting findings that, although preliminary, reinforce the idea that dynamical behaviour in tertiary amines is strongly influenced by the extent to which the lone pair on the N atom is able to interact with nearby unsaturated functional groups.

To further extend the theoretical characterization of our systematically varied systems we have evaluated the isotropic invariant of the second-moment of charge tensor relative to the $S_0$ ground state $\Delta < r_{iso}^2 >$ (a measure of the spatial extent of an electronic state) to compare the two extremes: the aromatic species *N*,*N*-DMA, and the fully saturated tertiary amine *N*,*N*-DMCHA. For the second moments we have used a slightly reduced basis set of

the aug-cc-pVDZ on N and C atoms, and the cc-pVDZ basis on hydrogens. As demonstrated previously, $\Delta < r_{iso}^2 >$ provides useful additional information for parametrizing the nature (and evolution) of electronic character, with Rydberg states typically exhibiting values that are somewhat larger than valence states (often by an order of magnitude or more).[6, 35, 38] We find here that the Rydberg-to-valence character evolution along the N-$CH_3$ stretch seen in Fig. 9 is also strongly reflected in the $\Delta < r_{iso}^2 >$ values, as illustrated in Fig. 10. In *N*,*N*-DMCHA it is a higher-lying (notionally) p-Rydberg state that undergoes a significant orbital size contraction but in *N*,*N*-DMA it is the 3s state that, instead, exhibits this behaviour.

## VII. CONCLUSION

Time-resolved photoelectron imaging readily reveals the presence of multiple non-adiabatic pathways in the aniline derivatives *N*,*N*-dimethylaniline (*N*,*N*-DMA) and 3,5-dimethylaniline (3,5-DMA) following excitation at 240 nm. The use of site-selective methylation, in conjunction with supporting *ab initio* calculations and the highly differential energy- and angle-resolved data afforded by our experimental approach, brings considerable new insight to the overall relaxation dynamics operating in these systems – which are good starting models for biological chromophores potentially involved in UV photoprotection. Detailed analysis of our data reveals decay of the mixed Rydberg/valence $S_2$ (3s/$\pi\sigma^*$) state in *N*,*N*-DMA likely proceeds via two competing pathways: internal conversion to the (much longer-lived) $S_1$ ($\pi\pi^*$) state or direct dissociation along the N-$CH_3$ coordinate. In 3,5-DMA, however, only the direct dissociation pathway (in this case N-H dissociation) appears to operate. This is rationalized in terms of changes in the relative rates of the two decay pathways upon methylation of the aromatic ring system – as strongly supported by the temporal evolution of the photoelectron angular distributions. Additionally, we see no clear evidence of the second excited $2\pi\pi^*$ state coupling non-adiabatically to the lower-lying $S_1$

($\pi\pi^*$) or $S_2$ ($3s/\pi\sigma^*$) states. This, in turn, suggests that the ultrafast decay of the $2\pi\pi^*$ state may occur via a route other than internal conversion to the $S_0$ state – a pathway previously suggested to operate in aniline. We speculate that the role of several Rydberg states predicted to sit energetically just below the $2\pi\pi^*$ state may ultimately prove to be a key factor here. More generally our findings, when taken along with other recent results for several aliphatic amine species, also highlight more general questions about the nature of electronic character evolution in mixed Rydberg-valence states as a function of certain key bond extensions. Exploring these ideas computationally for a systematically varied series of tertiary amines reveals that that dynamical behaviour exhibited by these systems is strongly influenced by the extent to which the N atom lone pair is able to interact with nearby unsaturated functional groups. We aim to explore these effects in more detail, both experimentally and theoretically, in the near future.

## ACKNOWLEDGEMENTS

This work was supported by Engineering and Physical Sciences Research Council (EPSRC) Grant No. EP/K021052/1. M.J.P. is supported by the European Research Council under the European Union's Seventh Framework Programme (FP7/2007-2013)/ERC Grant No. 258990. M.M.Z. and S.W.C thank Heriot-Watt University for PhD funding. We also acknowledge several collaborators who have contributed in numerous ways to various aspects of the work discussed here; J.O.F Thompson, E. A Burgess, L. B. Klein and T. I. Sølling.

## REFERENCES


1. C. E. Crespo-Hernández, B. Cohen, P. M. Hare and B. Kohler, *Chem. Res.*, 2004, **104**, 1977.
2. C. S. Cockell and J. Knowland, *Biol. Rev.*, 1999, **74**, 311.
3. M. N. R. Ashfold, G. A. King, D. Murdock, M. G. D. Nix, T. A. A. Oliver and A. G. Sage, *Phys. Chem. Chem. Phys.*, 2010, **12**, 1218.
4. G. M. Roberts and V. G. Stavros, *Chem. Sci.*, 2014, **5**, 1698.
5. I. Cnossen, J. Sanz-Forcada, F. Favata, O. Witasse, T. Zegers and N. F. Arnold, *J. Geophys,. Res.*, 2007, **112**, E02008.
6. J. O. F. Thompson, L. Saalbach, S. W. Crane, M. J. Paterson and D. Townsend, *J. Chem. Phys.*, 2015, **142**, 114309.
7. O. M. Kirkby, M. Sala, G. Balerdi, R. de Nalda, L. Bañares, S. Guérin and H. H. Fielding, *Phys. Chem. Chem. Phys.*, 2015, **17**, 16270.
8. M. Sala, O. M. Kirkby, S. Guérin and H. H. Fielding, *Phys. Chem. Chem. Phys.*, 2014, **16**, 3122.
9. J. O. F. Thompson, R. A. Livingstone and D. Townsend, *J. Chem. Phys.*, 2013, **139**, 034316.
10. R. Spesyvtsev, O. M. Kirkby, M. Vacher and H. H. Fielding, *Phys. Chem. Chem. Phys.*, 2012, **14**, 9942.
11. R. Spesyvtsev, O. M. Kirkby and H. H. Fielding, *Faraday Discuss.*, 2012, **157**, 165.
12. G. M. Roberts, C. A. Williams, J. D. Young, S. Ullrich, M. J. Paterson and V. G. Stavros, *J. Am. Chem. Soc.*, 2012, **134**, 12578.
13. R. Montero, A. Peralta-Conde, V. Ovejas, R. Martínez, F. Castaño and A. Longarte, *J. Chem. Phys.*, 2011, **135**, 054308.
14. G. A. King, T. A. A. Oliver and M. N. R. Ashfold, *J. Chem. Phys.*, 2010, **132**, 214307.
15. X.-J. Hou, P. Quan, T. Höltzl, T. Veszprémi and M. T. Nguyen, *J. Phys. Chem. A*, 2005, **109**, 10396.
16. Y. Honda, M. Hada, M. Ehara and H. Nakatsuji, *J. Chem. Phys.*, 2002, **117**, 2045.
17. F. Wang, S. P. Neville, R. Wang and G. A. Worth, *J. Phys. Chem. A*, 2013, **117**, 7298.
18. J. O. F. Thompson, L. B. Klein, T. I. Sølling, M. J. Paterson and D. Townsend, *Chem. Sci.*, 2016, **7**, 1826.
19. L. B. Klein, T. J. Morsing, R. A. Livingstone, D. Townsend and T. I. Sølling, *Phys. Chem. Chem. Phys.*, 2016, **18**, 9715.
20. L. B. Klein, J. O. F. Thompson, S. W. Crane, L. Saalbach, T. I. Sølling, M. J. Paterson and D. Townsend, *In preparation*.
21. R. A. Livingstone, J. O. F. Thompson, M. Iljina, R. J. Donaldson, B. J. Sussman, M. J. Paterson and D. Townsend, *J. Chem. Phys.*, 2012, **137**, 184304.
22. U. Even, J. Jortner, D. Noy, N. Lavie and C. Cossart-Magos, *J. Chem. Phys.*, 2000, **112**, 8068.
23. A. T. J. B. Eppink and D. H. Parker, *Rev. Sci. Instrum.*, 1997, **68**, 3477.
24. L. Szepes, G. Distefano and S. Pignataro, *Ann. Chim.*, 1974, **64**, 159.
25. J. P. Maier and D. W. Turner, *J. Chem. Soc. Faraday Trans. 2*, 1973, **69**, 521.
26. T. Suzuki, *Annu. Rev. Phys. Chem.*, 2006, **57**, 555.
27. K. L. Reid, *Annu. Rev. Phys. Chem.*, 2003, **54**, 397.
28. Gaussian 09, Revision D.01, M. J. Frisch, G. W. Trucks, H. B. Schlegel, G. E. Scuseria, M. A. Robb, J. R. Cheeseman, G. Scalmani, V. Barone, B. Mennucci, G. A. Petersson, H. Nakatsuji, M. Caricato, X. Li, H. P. Hratchian, A. F. Izmaylov, J.

Bloino, G. Zheng, J. L. Sonnenberg, M. Hada, M. Ehara, K. Toyota, R. Fukuda, J. Hasegawa, M. Ishida, T. Nakajima, Y. Honda, O. Kitao, H. Nakai, T. Vreven, J. A. Montgomery, Jr., J. E. Peralta, F. Ogliaro, M. Bearpark, J. J. Heyd, E. Brothers, K. N. Kudin, V. N. Staroverov, R. Kobayashi, J. Normand, K. Raghavachari, A. Rendell, J. C. Burant, S. S. Iyengar, J. Tomasi, M. Cossi, N. Rega, J. M. Millam, M. Klene, J. E. Knox, J. B. Cross, V. Bakken, C. Adamo, J. Jaramillo, R. Gomperts, R. E. Stratmann, O. Yazyev, A. J. Austin, R. Cammi, C. Pomelli, J. W. Ochterski, R. L. Martin, K. Morokuma, V. G. Zakrzewski, G. A. Voth, P. Salvador, J. J. Dannenberg, S. Dapprich, A. D. Daniels, Ö. Farkas, J. B. Foresman, J. V. Ortiz, J. Cioslowski, and D. J. Fox, Gaussian, Inc., Wallingford CT, 2009.

29. R. Scheps, D. Florida and S. A. Rice, *J. Chem. Phys.*, 1974, **61**, 1730.
30. B. Kim, C. P. Schick and P. M. Weber, *J. Chem. Phys.*, 1995, **103**, 6903.
31. G. Wu, P. Hockett and A. Stolow, *Phys. Chem. Chem. Phys.*, 2011, **13**, 18447.
32. Y.-I. Suzuki, T. Horio, T. Fuji and T. Suzuki, *J. Chem. Phys.*, 2011, **134**, 184313.
33. C. Z. Bisgaard, O. J. Clarkin, G. Wu, A. M. D. Lee, O. Gessner, C. C. Hayden and A. Stolow, *Science*, 2009, **323**, 1464.
34. We note that additional dynamical factors (other than non-adiabatic coupling) may also influence/convolute the observed form of the PADs. Primarily these are (i) changes in the relative phases and amplitudes of the outgoing photoelectron partial waves due to conformational rearrangement modifying the scattering dynamics off the non-spherical ion core potential and (ii) major changes in orbital character that may occur as a function of nuclear coordinates (for example, the signigicant Rydberg to valence evolution seen here in the $S_2$ ($3s/\pi\sigma^*$) state) . Point (i) is generally expected to be relatively small and point (ii) is not expected to be significnat for the predominanlty valence $S_1$ ($\pi\pi^*$) state considered here.
35. M. M. Zawadzki, J. O. F. Thompson, E. A. Burgess, M. J. Paterson and D. Townsend, *Phys. Chem. Chem. Phys.*, 2015, 1**7**, 26659.
36. R. Spesyvtsev, PhD Thesis, University College London, 2013.
37. Using linear response CCSD with a mixed basis (aug-cc-pVDZ pn C and N, and cc-pVDZ on H). Polarizability volumes at ground state equilibrium geometries are 2.04 $Å^3$ for $S_1(\pi\pi^*)$ and 26.08 $Å^3$ for $2\pi\pi^*$.
38. H. Reisler and A. I. Krylov, *Int. Rev. Phys. Chem.*, 2009, **28**, 267.

## TABLE CAPTIONS

**Table I:** EOM-CCSD/aug-cc-pVDZ vertical excitation energies ($\Delta E$) and oscillator strengths ($f$) obtained for *N*,*N*-DMA and 3,5-DMA, along with corresponding state assignments. For more details see the main text. Note that for *N*,*N*-DMA the ordering of the first ππ* and 3s/πσ* states depend delicately on electron correlation, with a connected triples correction changing the ordering (see Ref. 6). In the absence of any experimental data confirming the true ordering of these states, the $S_1(\pi\pi^*)$ and $S_2(3s/\pi\sigma^*)$ labels will be used throughout for both systems for clarity in subsequent discussions. The p manifold is heavily mixed with orbitals directed away from the *x*,*y* and *z* molecular axes. As such, no specific assignments are given.

**Table I**

| | | ΔE (eV) (CCSD)[a] | *f* (CCSD) |
|---|---|---|---|
| ***N*,*N*-Dimethylaniline** | | | |
| $^1A'$ | $S_0$[b] | 0 | - |
| $1\ ^1A'$ | $S_2(3s/\pi\sigma^*)$ | 4.55 | 0.0231 |
| $1\ ^1A''$ | $S_1(\pi\pi^*)$ | 4.59 | 0.0406 |
| $2\ ^1A'$ | 3p | 5.14 | 0.0007 |
| $2\ ^1A''$ | 3s | 5.17 | 0.0145 |
| $3\ ^1A'$ | 3p | 5.41 | 0.0119 |
| $4\ ^1A'$ | $2\pi\pi^*$ | 5.49 | 0.2441 |
| **3,5-Dimethylaniline** | | | |
| $^1A'$ | $S_0$[b] | 0 | - |
| $1\ ^1A''$ | $\pi\pi^*$ | 4.68 | 0.0247 |
| $1\ ^1A'$ | $3s/\pi\sigma^*$ | 4.80 | 0.0034 |
| $2\ ^1A'$ | 3s | 5.49 | 0.0089 |
| $2\ ^1A''$ | 3p | 5.55 | 0.0004 |
| $3\ ^1A'$ | $2\pi\pi^*$ | 5.65 | 0.1135 |
| $4\ ^1A'$ | 3p | 5.92 | 0.0037 |

[a] aug-cc-pVDZ basis set for response properties
[b] $S_0$ geometries from B3LYP/aug-cc-pVTZ optimisation in $C_s$ symmetry

## FIGURE CAPTIONS

**Figure 1:** UV vapour-phase room temperature absorption spectra of *N*,*N*-dimethylaniline (*N*,*N*-DMA) and 3,5-dimethylaniline (3,5-DMA) (schematic structures of which are inset) recorded using a commercial bench-top spectrophotometer (Shimadzu UV-2550). Vertical dashed lines denote the pump and probe wavelengths used in our TRPEI measurements. Equivalent data recorded for aniline is also included for comparison.

**Figure 2:** (1 + 1′) photoelectron images obtained for *N*,*N*-DMA and 3,5-DMA at selected pump-probe delay times following 240 nm excitation and subsequent ionization using 308 nm. Time-invariant pump-alone and probe-alone signals have been subtracted and the images are 4-fold symmetrised. The (linear) polarization direction of the pump and probe beams is vertical with respect to the figure. The left half of the images show the processed data obtained following application of the matrix inversion approach described in Ref. 21.

**Figure 3:** Time-dependent photoelectron spectra of *N*,*N*-DMA, and 3,5-DMA obtained using a 240 nm pump/308 nm probe. For clear display of the dynamics over all temporal ranges, the time axis is linear to +500 fs and logarithmic between +500 fs and +100 ps. The data are partitioned into 0.025 eV energy bins. Also shown is the fit to the 3,5-DMA data (obtained using the procedure described in the main text) along with the associated residuals (i.e., the fit subtracted from the raw data).

**Figure 4:** Decay associated spectra (DAS) obtained from a global multi-exponential fit to the data presented in Fig. 4. For additional details, see the main text. Uncertainties quoted are 1$\sigma$ values and the data are partitioned into 0.025 eV energy bins. Vertical dashed lines denote predicted maximum photoelectron kinetic energy cut-offs based on the central pump and probe wavelengths and the adiabatic ionization potentials (7.26 eV and 7.48 eV for *N*,*N*-DMA, and 3,5-DMA, respectively, as determined in Ref. 6).

**Figure 5:** (Left) anisotropy parameters $\beta_2$ and $\beta_4$ as a function of pump-probe delay averaged over the 0.05-0.70 eV photoelectron kinetic energies region following 240 nm excitation/308 nm ionization of *N*,*N*-DMA and 3,5-DMA. The time axes are linear to +500 fs and logarithmic between +500 fs and +100 ps. The data were partitioned into 0.025 eV energy bins for initial anisotropy fits (before averaging), and the error bars represent one standard deviation. Fits were performed over the angular region $5^\circ \leq \theta \leq 90^\circ$ to eliminate uncertainties from centre-line noise present in the Abel-inverted images (see Fig. 2). (Right) anisotropy parameters $\beta_2$ and $\beta_4$ as a function of photoelectron kinetic energy at zero pump-probe delay (data points) superimposed over the corresponding photoelectron spectrum (grey line).

**Figure 6:** EOM-CCSD/aug-cc-pVDZ potential energy cuts along the N–H stretching coordinate (3,5-DMA) and the N–$CH_3$ stretching coordinate (*N*,*N*-DMA) for the $S_0$ ground state and several low-lying electronically excited singlet states. For additional details, see the main text. The p manifold is heavily mixed with orbitals directed away from the *x*,*y* and *z* molecular axes. As such, no specific assignments are given.

**Figure 7:** 2D time-dependent photoelectron spectra of piperidene (top) and *N*-methylpyrrolidine (bottom) obtained using a similar TRPEI setup to that described in the Experimental section using a 200 nm pump and 267 nm probe. The time axis is linear to +1 ps and then logarithmic beyond this point. The intensity colour map is presented on a natural logarithmic scale based on the output directly obtained from the CCD camera used to record the raw photoelectron image data. The *N*-methylpyrrolidine and piperidene data are adapted from Refs 18 and 20, respectively.

**Figure 8:** Schematic depictions of *N*,*N*-dimethylcyclohexylamine (*N*,*N*-DMCHA), *N*,*N*-dimethyl-1-cyclohexen-1-amine (*N*,*N*-DM-1-CHA), *N*,*N*-dimethyl-2,4-cyclohexadiene-1-

amine (*N*,*N*-DM-2,4-CHA) and *N*,*N*-dimethyl-1,3-cyclohexadiene-1-amine (*N*,*N*-DM-1,3-CHA).

**Figure 9:** EOM-CCSD/aug-cc-pVDZ potential energy cuts along the N-$CH_3$ stretching coordinate of *N*,*N*-DMCHA (top left), *N*,*N*-DM-1-CHA (top right), *N*,*N*-DM-2,4-CHA (bottom left) and *N*,*N*-DM-1,3-CHA (bottom right). For additional details, see the main text. The p manifold is heavily mixed with orbitals directed away from the *x*,*y* and *z* molecular axes. As such, no specific assignments are given.

**Figure 10:** Evolution of the excited-state second-moment of the electronic charge distribution with respect to the ground state $\Delta < r_{iso}^2 >$ in *N*,*N*-DMCHA and *N*,*N*-DMA as a function of N-$CH_3$ bond extension. For additional details see the main text. Data for only one of the 3p states showing no significant valence evolution is included.

**Figure 1**

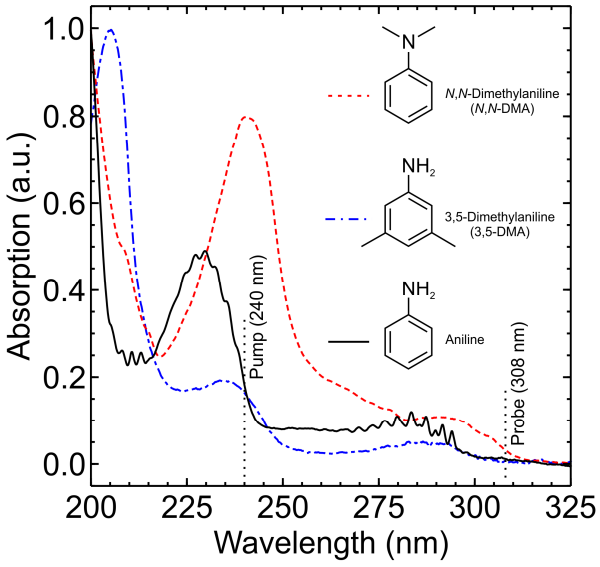
Absorption (a.u.)
Wavelength (nm)
1.0
0.8
0.6
0.4
0.2
0.0
200
225
250
275
300
325
N
N,N-Dimethylaniline
(N,N-DMA)
NH2
3,5-Dimethylaniline
(3,5-DMA)
NH2
Aniline
Pump (240 nm)
Probe (308 nm)

**Figure 2**

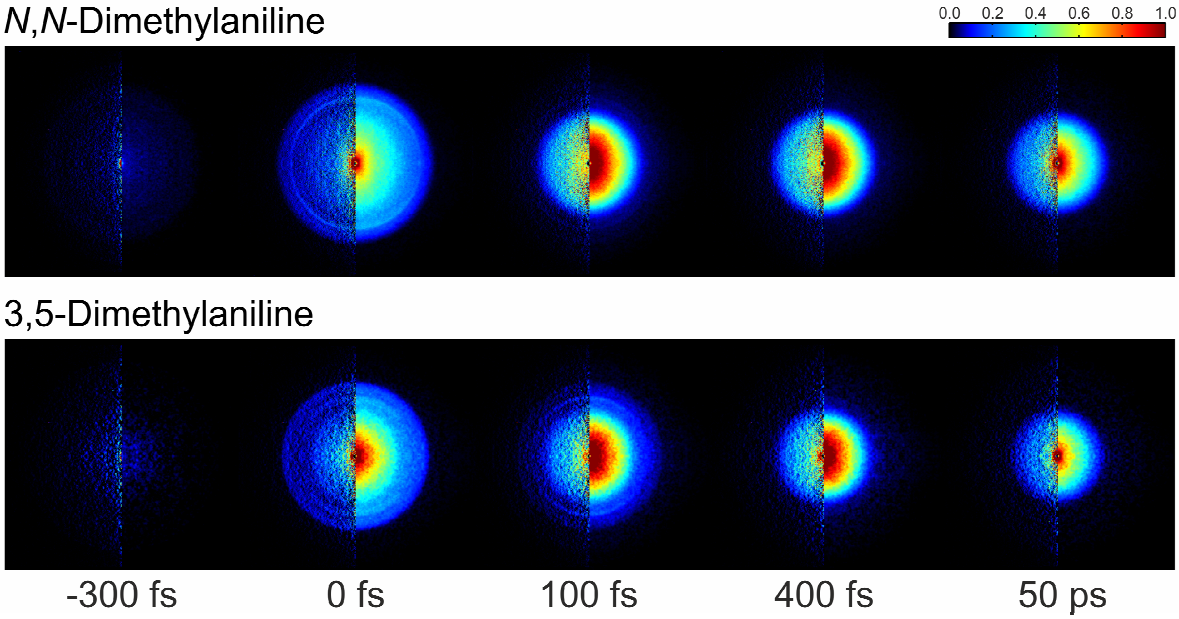
*N*,*N*-Dimethylaniline
0.0 0.2 0.4 0.6 0.8 1.0
3,5-Dimethylaniline
-300 fs
0 fs
100 fs
400 fs
50 ps

**Figure 3**

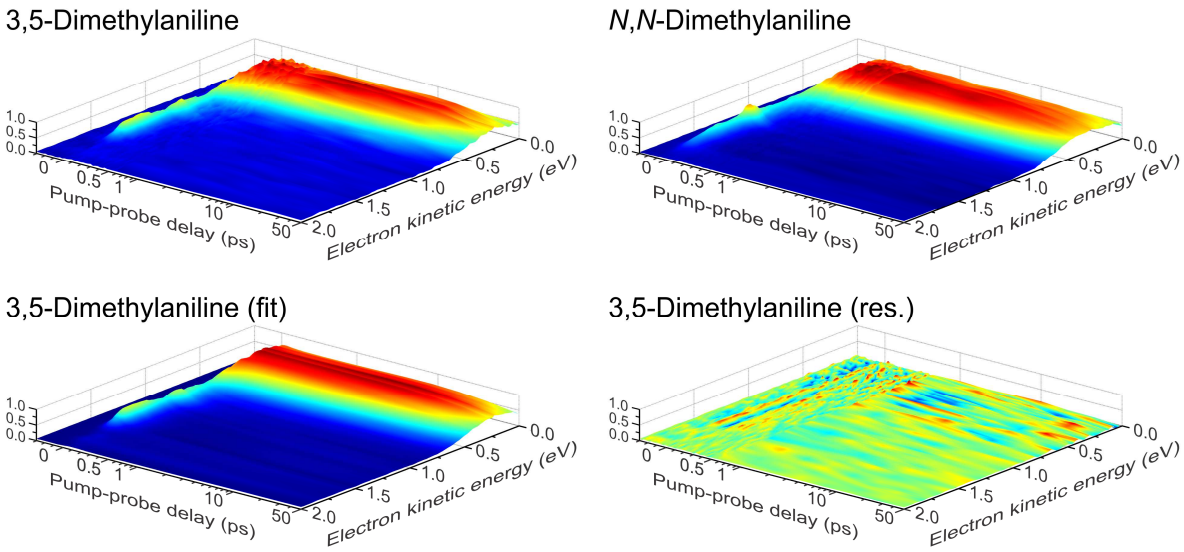
3,5-Dimethylaniline
N,N-Dimethylaniline
3,5-Dimethylaniline (fit)
3,5-Dimethylaniline (res.)
Pump-probe delay (ps)
Electron kinetic energy (eV)
0
0.5
1
10
50
2.0
1.5
1.0
0.5
0.0
1.0
0.5
0.0

**Figure 4**

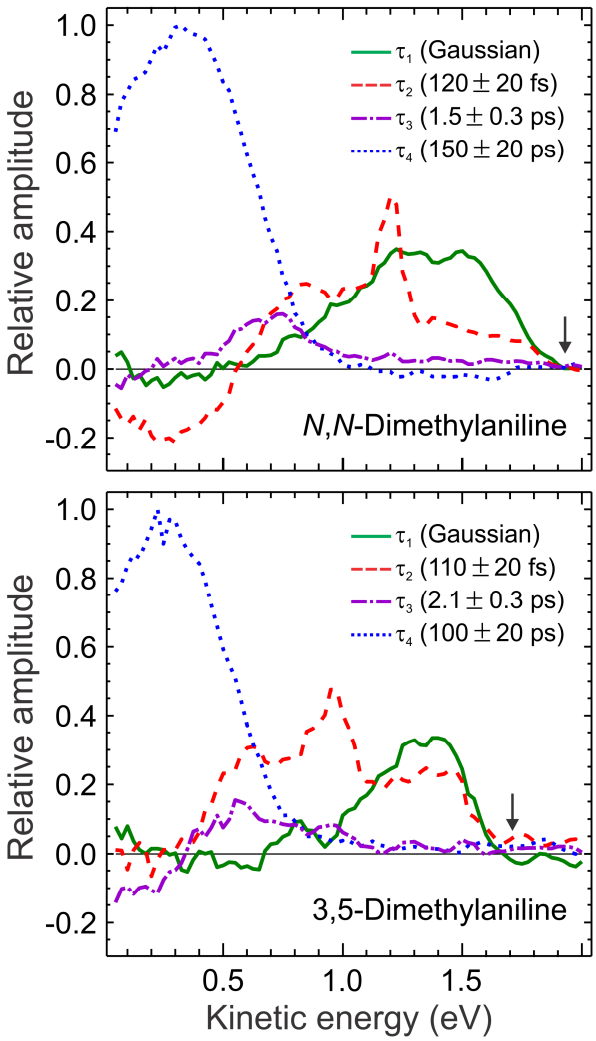
Relative amplitude
1.0
0.8
0.6
0.4
0.2
0.0
-0.2
τ1 (Gaussian)
τ2 (120 ± 20 fs)
τ3 (1.5 ± 0.3 ps)
τ4 (150 ± 20 ps)
N,N-Dimethylaniline
Relative amplitude
τ1 (Gaussian)
τ2 (110 ± 20 fs)
τ3 (2.1 ± 0.3 ps)
τ4 (100 ± 20 ps)
3,5-Dimethylaniline
0.5
1.0
1.5
Kinetic energy (eV)

**Figure 5**

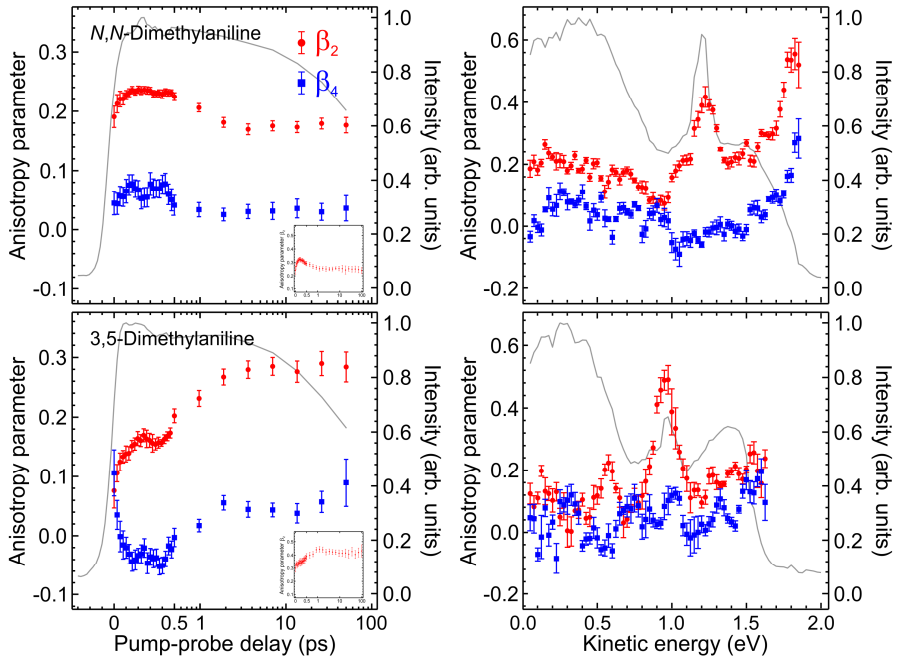
N,N-Dimethylaniline
β2
β4
3,5-Dimethylaniline
Anisotropy parameter
Intensity (arb. units)
Pump-probe delay (ps)
Kinetic energy (eV)

**Figure 6**

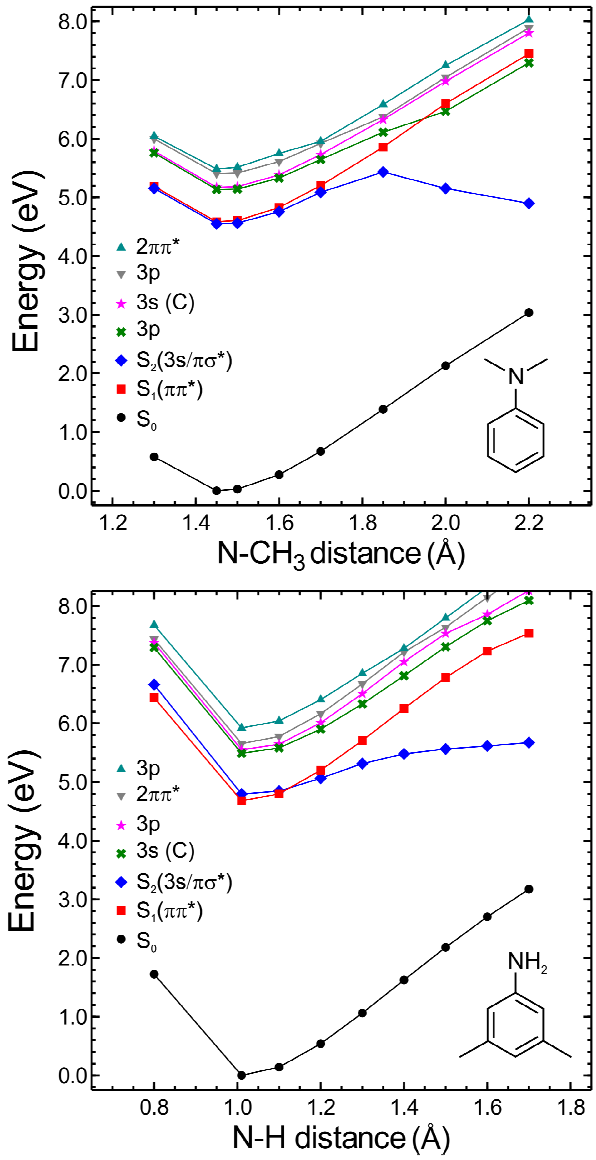
Energy (eV)
N-CH3 distance (Å)
2ππ*
3p
3s (C)
3p
S2(3s/πσ*)
S1(ππ*)
S0
N
Energy (eV)
N-H distance (Å)
3p
2ππ*
3p
3s (C)
S2(3s/πσ*)
S1(ππ*)
S0
NH2

**Figure 7**

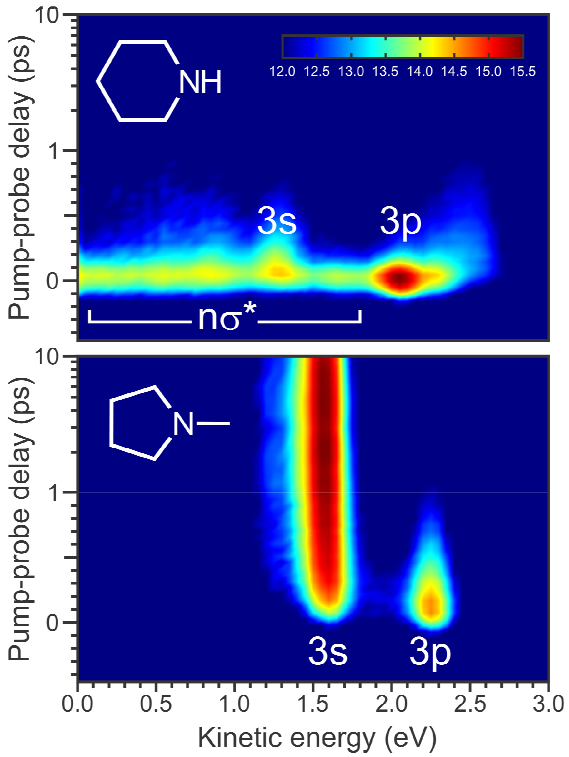
NH
12.0 12.5 13.0 13.5 14.0 14.5 15.0 15.5
3s
3p
nσ*
N—
3s
3p
Pump-probe delay (ps)
Pump-probe delay (ps)
10
1
0
10
1
0
0.0 0.5 1.0 1.5 2.0 2.5 3.0
Kinetic energy (eV)

**Figure 8**

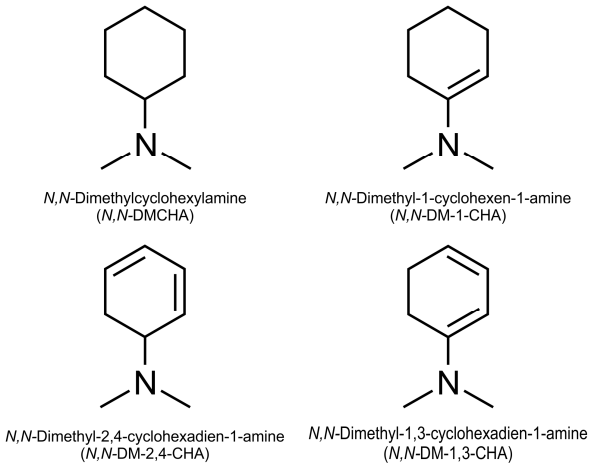
N
N,N-Dimethylcyclohexylamine
(N,N-DMCHA)
N
N,N-Dimethyl-1-cyclohexen-1-amine
(N,N-DM-1-CHA)
N
N,N-Dimethyl-2,4-cyclohexadien-1-amine
(N,N-DM-2,4-CHA)
N
N,N-Dimethyl-1,3-cyclohexadien-1-amine
(N,N-DM-1,3-CHA)

**Figure 9**

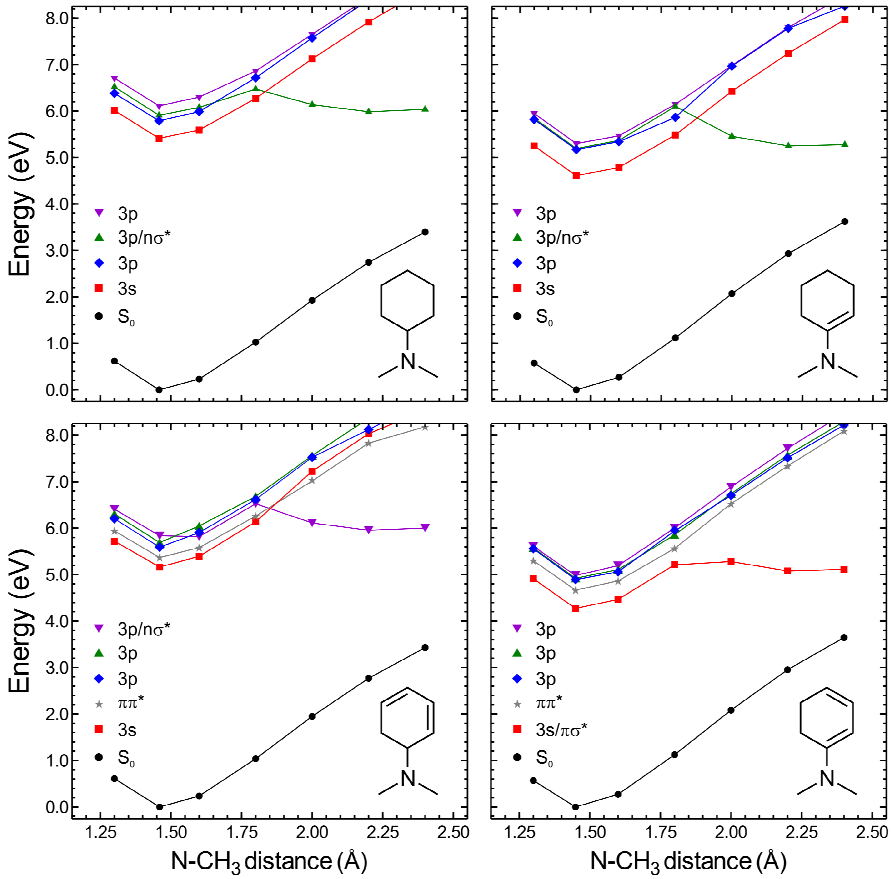
Energy (eV)
N-CH3 distance (Å)
3p
3p/nσ*
3p
3s
S0
3p/nσ*
3p
ππ*
3s
3p
3p
3p
ππ*
3s/πσ*

**Figure 10**

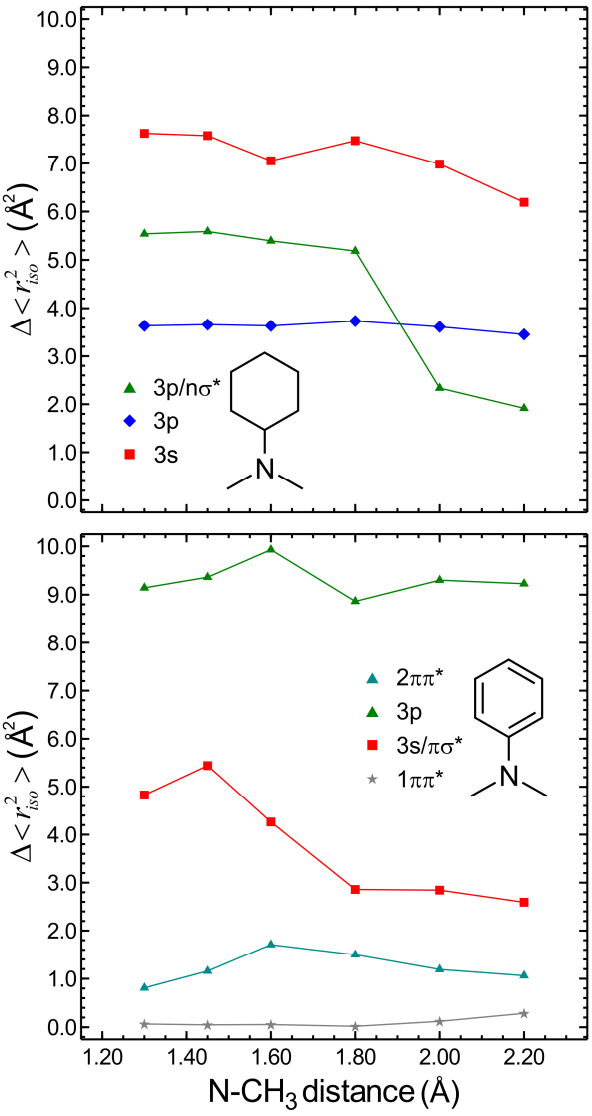
10.0
9.0
8.0
7.0
6.0
5.0
4.0
3.0
2.0
1.0
0.0
$\Delta < r_{iso}^2 >$ (Å$^2$)
3p/nσ*
3p
3s
N
2ππ*
3p
3s/πσ*
1ππ*
1.20
1.40
1.60
1.80
2.00
2.20
N-CH$_3$ distance (Å)

## Graphical Abstract